



## Hierarchical Ag-Cu interfaces promote C-C coupling in tandem CO<sub>2</sub> electroreduction

Zhizhou Cai <sup>a,1</sup>, Ning Cao <sup>a,1</sup>, Fanxing Zhang <sup>a</sup>, Xiangzhou Lv <sup>b</sup>, Ke Wang <sup>a</sup>, Yi He <sup>a</sup>, Yao Shi <sup>a</sup>, Hao Bin Wu <sup>b,\*</sup>, Pengfei Xie <sup>a,\*</sup>

<sup>a</sup> College of Chemical and Biological Engineering, Zhejiang University, Hangzhou 310027, China

<sup>b</sup> Institute for Composites Science Innovation (InCSI) and State Key Laboratory of Silicon Materials, School of Materials Science and Engineering, Zhejiang University, Hangzhou 310027, China



### ARTICLE INFO

**Keywords:**  
Tandemly electrocatalytic CO<sub>2</sub> reduction  
Ethanol  
Hierarchical interfaces  
C-C coupling  
Interface confinement

### ABSTRACT

Electrocatalytic CO<sub>2</sub> reduction into ethanol driven by renewable energy represents a promising strategy for energy storage and mitigation of global warming, but it has remained challenging to gain high activity and selectivity of ethanol. Here we take advantage of atomic arrangement in immiscible Ag-Cu composite during annealing and establish hierarchical interfaces in the obtained core-shell catalyst. The atomic Ag-Cu interactions increase electrochemical surface area and expedite charge dynamics, resulting in an unprecedented electrocatalytic performance with the faradaic efficiency of C<sub>2+</sub> products, ethanol as 80.2 %, 52.6 % and the current density of ~320 mA cm<sup>-2</sup> at -1.0 V (versus reversible hydrogen electrode). Moreover, the Ag-Cu catalyst exhibits a notable stability for ~60 h. Mechanism studies reveal that local CO intermediates preferentially accumulate on the core, then migrate to the continuous Cu surface for C-C coupling energy-favorably toward ethanol. Our work highlights a novel design principle as interface engineering for advanced tandem electrocatalysts.

### 1. Introduction

The continuous fossil consumption has been depleting the energy reserves and elevating the level of anthropogenic CO<sub>2</sub> emission, causing climate change. Electrocatalytic reduction of CO<sub>2</sub> (CO<sub>2</sub>RR) driven by green energy (e.g., solar, wind) into valuable feedstocks and fuels provides a promising strategy to mitigate the global warming and store the intermittent renewable energy [1–3]. In the past decade, CO<sub>2</sub>RR toward single carbon (C<sub>1</sub>) products gains remarkable progress, especially for carbon monoxide [4], methane and formic acid [5,6]. While multi-carbon compounds (C<sub>2+</sub>, e.g., ethanol) are attracting more attention because of their higher value and energy density [7–9].

Owing to the unique binding energy with key intermediates involved in CO<sub>2</sub>RR (e.g., \*CO and \*H), only copper (Cu) exhibits distinctive catalytic properties for the conversion of CO<sub>2</sub> into C<sub>2+</sub> products and suppresses the competitive hydrogen evolution reaction (HER) [10]. However, the sluggish kinetics of C-C coupling impede its further application due to the limited faradaic efficiency (FE) of different C<sub>2+</sub> products and low current density [11]. Thus, tremendous efforts have

been devoted to improving the selectivity of particular C<sub>2+</sub> [12], such as alloying [13,14], surface doping [15–18], and interface engineering [19–21]. Recently, tandem catalyst [22–24] has emerged as a promising design principle to promote C<sub>2+</sub> [25]. In this principle, the CO intermediates are generated on the domain, such as Ag [23], Au [26], Zn [27,28], Fe [29,30], which is integrated with Cu, subsequently spilled over to Cu site for C-C coupling. Among these catalysts, bimetallic CuAg ensembles stand out with excellent FE of total C<sub>2+</sub> products as 30~85 % at -0.7 ~ -1.2 V vs. RHE (all potentials in this study are with respect to this reference). However, the FE of ethanol (C<sub>2</sub>H<sub>5</sub>OH) is yet obtained with considerably lower efficiencies (FE < 41 % [31]), which is more energy intensive and easy to store compared to ethylene (C<sub>2</sub>H<sub>4</sub>) [32].

Experimental [32] and theoretical [33] studies have demonstrated that the hydrogenation of key intermediates (e.g., \*COCHO) derived from C-C coupling determines the selectivity of ethylene and ethanol, which relies on the controlling and optimization of the binding strength of reaction intermediates on the catalyst surfaces. Interface engineering has been proposed to modulate the adsorption of reaction species by utilizing the synergistic interaction between two intimate elements in the

\* Corresponding authors.

E-mail addresses: [hbwu@zju.edu.cn](mailto:hbwu@zju.edu.cn) (H. Bin Wu), [pfxie@zju.edu.cn](mailto:pfxie@zju.edu.cn) (P. Xie).

<sup>1</sup> These authors contributed equally to this work.

catalysts (e.g., Cu and Ag) [20,31]. However, it is challenging to maximize the Cu and Ag interfaces at the atomic level, because they are thermodynamically immiscible over almost all compositions at room temperature [34,35].

Here we report on the synthesis of core-shell Ag-Cu schemes (core: Cu<sub>2</sub>O/Ag composite, shell: CuO layer) for CO<sub>2</sub>RR selectively to ethanol by adjusting the loadings of Cu organometallic complex on colloidal Ag NPs and annealing in air. The hierarchical interface is established at the atomic structure including the interactions between Cu and Ag within the core and the interactions between the core and shell (Cu layer), as characterized by using scanning transmission electron microscopy (STEM), X-ray photoemission spectroscopy (XPS) and X-Ray Diffraction (XRD). The core-shell Ag-Cu catalyst exhibits superior catalytic performance and excellent stability. The control experiments, *in situ* Raman and density functional theory calculations (DFT) reveal a mechanism that the energy-favorable CHO-CHO coupling at the interfaces between core-shell structures favors the formation of ethanol.

## 2. Experimental section

### 2.1. Materials

All chemicals were analytical reagents and were used without further purification. Silver citrate was purchased from Shanghai Maclean Biochemical Technology Co., Ltd. and PVP was purchased from Aladdin. All other reagents were purchased from China National Pharmaceutical Group Chemical Reagent Co. Ultra-pure water was used throughout the experiments.

### 2.2. Synthesis of Ag NPs

Silver citrate was added in 150 mL deionized water containing 5 g PVP to form a 1000 mg L<sup>-1</sup> silver citrate solution. Under the condition of vigorous stirring, 60 mg ascorbic acid aqueous solution was gradually dropped into the silver citrate solution, and stirred for 1 h. The obtained black solution was centrifuged to obtain Ag particles, which were washed three times alternately with water and ethanol.

### 2.3. Synthesis of Ag-Cu catalyst

The copper organometallic precursor (see the synthesis details in Supporting Information) was homogeneously dispersed on Ag NPs in methanol solution by sonication and stirring, and then the solution was evaporated and calcined in a muffle furnace at 250 °C for 10 h to obtain the Ag-Cu catalyst.

### 2.4. Characterization and Instruments

The morphology of these materials was studied on TEM (JEOL JEM-2100F). The crystal structures of the materials were characterized by XRD on a Bruker (APEXII) diffractometer. The elemental analysis was tested by ICP-OES using an Agilent 720ES (OES). XPS tests were performed on a Thermo Scientific ESCALAB Xi+ spectrometer using Al K $\alpha$  radiation (1486.6 eV). The carbon peak at 284.8 eV was used as a reference to correct for charging effects. The operando Raman spectroscopy was conducted in 1 M KOH aqueous solution using a flow-cell on a confocal Raman spectrometer (Renishaw). The spectra were collected during the chronoamperometric i-t test for 2 min at each potential.

### 2.5. Electrochemical experiments

All electrocatalytic experiments were performed on an electrochemical workstation (CH Instruments, Inc., USA). The flow cell configuration was consisted of a catalyst-loaded GDE (1 × 3 cm) as the working electrode, a proton exchange membrane (Nafion 115, DuPont),

and an iridium-plated titanium sheet (1 × 3 cm) as the anode. Hg/HgO electrode was used as the reference electrode. The GDEs were prepared by drop-coating method. 10 mg of catalyst was dispersed in 670 μL water and 30 μL Nafion solution (5 wt. %), then sonicated for 30 min to obtain a homogeneous slurry. This mixture was applied dropwise on the gas diffusion layer with catalyst loading of 1 mg cm<sup>-2</sup>. The electrolyte (3 M KOH) was circulated at a flow rate of 10 mL min<sup>-1</sup> using a peristaltic pump. High pure CO<sub>2</sub> was introduced into the flow cell for 20 min at a flow rate of 15 mL min<sup>-1</sup> prior to testing.

Cyclic voltammetry (CV) was applied before the electrochemical experiments at a scan rate of 50 mV s<sup>-1</sup> between 0 V to -2.0 V versus Hg/HgO for 20 sweep segments. Linear sweep voltammetry (LSV) curves was applied at a scan rate of 50 mV s<sup>-1</sup>. All potentials were converted to RHE values by the following equation:

$$E_{\text{RHE}} (\text{V}) = E_{\text{Hg/HgO}} (\text{V}) + 0.098 \text{ V} + (0.0592 \text{ V} \times \text{pH}) \quad (1)$$

After 15 min of stabilization at each potential, gas phase and liquid phase samples were collected. The gas phase products of the constant potential tests performed by using a gas chromatograph (GC; Superlab Smart GC) equipped with a packed column (Porapak N 80/100 mesh), a thermal conductivity detector (TCD; for H<sub>2</sub>), and a flame ionization detector (FID; for CO, CH<sub>4</sub> and C<sub>2</sub>H<sub>4</sub>). The liquid products were analyzed by <sup>1</sup>H NMR (Bruker 600 M Hz).

The half-cell EE (CEE) was calculated on the basis of the cathodic CO<sub>2</sub>RR coupled with anodic water oxidation reaction (O<sub>2</sub> + 4 H<sup>+</sup> + 4e<sup>-</sup> ⇌ 2O<sub>2</sub>) by following literature [32] with the equation:

$$\text{EE} = \frac{E_{\text{OX}^0} - E_{\text{red}^0}}{E_{\text{OX}} - E_{\text{red}}} \times F E_{\text{ethanol}} \quad (2)$$

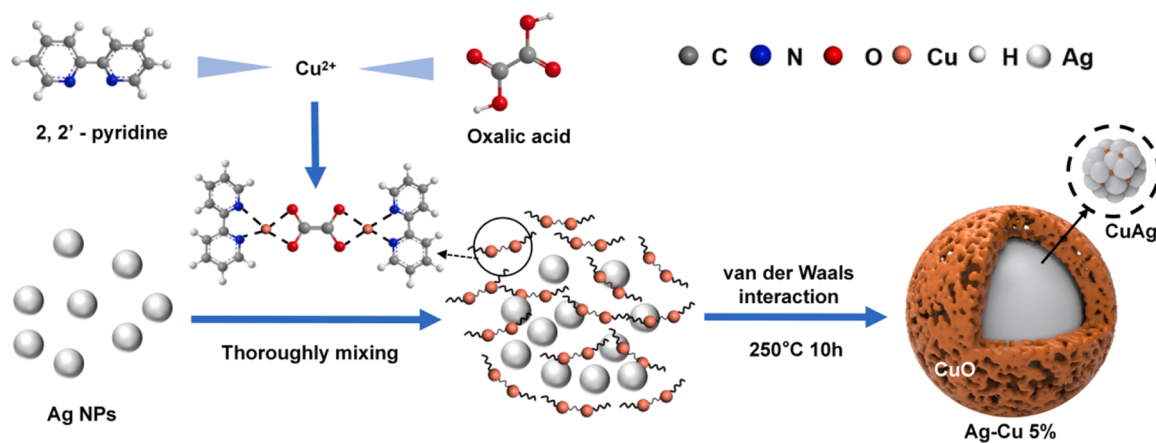
where E<sub>OX<sup>0</sup></sub> and E<sub>red<sup>0</sup></sub> are the thermodynamic potentials for H<sub>2</sub>O oxidation (1.23 V versus RHE) and CO<sub>2</sub>RR to ethanol (0.09 V versus RHE), respectively. E<sub>OX</sub> and E<sub>red</sub> are the applied potentials at anode and cathode.

## 3. Results and discussion

### 3.1. Synthesis and characterization of Ag-Cu ensembles

The pristine Ag-Cu composites were synthesized by thoroughly mixing the copper organometallic precursor ([Cu<sub>2</sub>(bpy)<sub>2</sub>(μ-ox)](OH)<sub>2</sub>) and colloidal Ag nanoparticles, subsequently annealed in air at 250 °C to remove the ligands (Scheme 1). Here, the organocuppper complex was derived by self-assembly [36] of Cu<sup>2+</sup> cations, 2,2'-bipyridine and oxalic acid, following the approach in our previous work [37] (Fig. S1). The silver nanoparticles with scales of ~50 nm (Fig. S2a) were prepared the reduction of Ag<sup>+</sup> by ascorbic acid in the presence of polyvinylpyrrolidone. In this synthesis, the as-prepared Ag-Cu mixtures are stabilized by the van der Waals interactions or hydrogen bond interactions between functional groups (e.g., O-H, C=O) on the surface of Cu and Ag domains (Fig. S1). The calcined Ag-Cu ensembles are denoted as Ag-Cu x, where x represents the nominal amount of Cu added (i.e., 2, 5 and 10 wt. %). The actual amounts of Cu were determined to be 1.9, 3.3 and 7.9 wt. % (Table S1) by using inductively coupled plasma optical emission spectrometry (ICP-OES). The bare silver, copper nanoparticles and Cu NPs (Fig. S2b) impregnated on Ag catalyst (Ag-CuNPs 5 %) were also synthesized, which serve as the controls in this study.

The morphologies and spatial configurations of Ag-Cu ensembles are studied by TEM analysis. Given the thermodynamic immiscibility between silver and copper, two phases are gradually segregated upon calcination and induces an atomic rearrangement governed by the different diffusion rate of Ag and Cu [38], as visualized in Fig. 1a-c. For Ag NPs, similar agglomerations are observed for three samples, which grow up to 100–150 nm (Fig. 1a-c). However, the distinguished reconstructions of copper atoms have occurred at different loadings as the result of Cu diffusion from the interior to the exterior, which allows to



Scheme 1. Schematic illustration of the synthetic route for core-shell Ag-Cu 5 %.

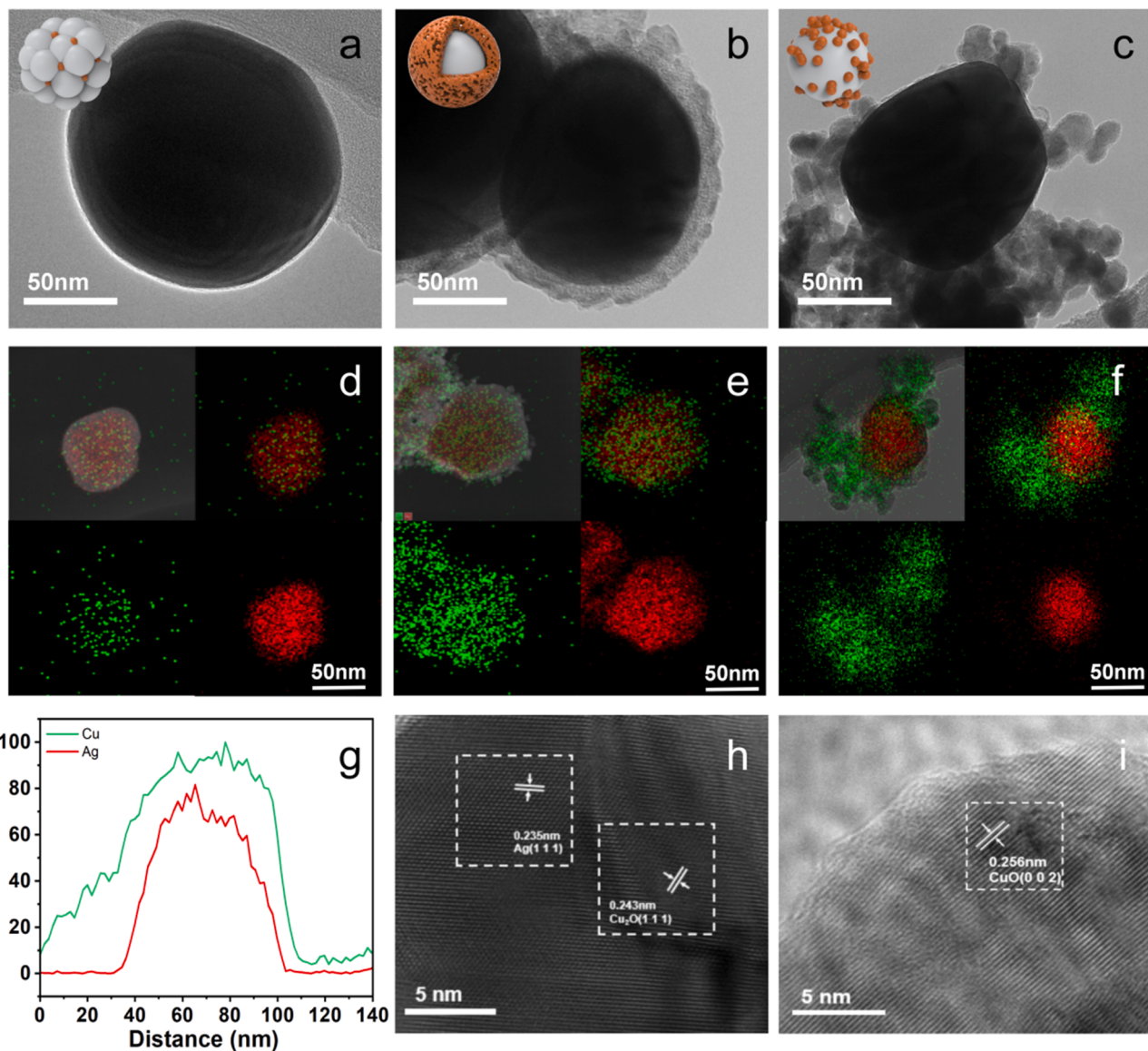


Fig. 1. Morphology characterizations of Ag-Cu catalysts. Typical transmission electron microscopy (TEM) images of (a) Ag-Cu 2 %, (b) Ag-Cu 5 %, (c) Ag-Cu 10 %. Representative elemental mappings images of (d) Ag-Cu 2 %, (e) Ag-Cu 5 %, (f) Ag-Cu 10 % (Cu:green, Ag:red). (g) Corresponding line scanning analysis and (h-i) High-resolution TEM images of Ag-Cu 5 %.

flexibly engineer the interface structures between silver and copper. As displayed by TEM images and the energy dispersive spectroscopy (EDS) mapping results, Ag-Cu 2 % has Cu well dispersed on silver NPs (Fig. 1a, d) while larger Cu NPs with 20–30 nm are shown on silver NPs for Ag-Cu 10 % (Fig. 1c, f), implying at higher loading most of Cu are aggregated during calcination. To be different, a core-shell structure is constructed only at Ag-Cu 5 % (Fig. 1b). The EDS mapping (Fig. 1e) and line-profile scanning across the particles (Fig. 1g) clearly exhibit that the core includes a silver and copper mixture and is entirely covered by uncompact copper shell with a thickness of 5–10 nm (Fig. 1b). The atomic resolution TEM imaging of Ag-Cu 5 % further measures two different lattice distances in the core, which are found to be 2.35 Å and 2.43 Å (Fig. 1h), corresponding to Ag (111) facet and Cu<sub>2</sub>O (111) facet, respectively, whereas the lattice spacing of Cu species in the shell as 2.56 Å is ascribed to CuO (002) (Fig. 1i). A lattice strain related to Ag (111) near multiple interfaces is noticed by 2.39–2.40 Å (versus 2.35 Å in bulk), proving the

strong interactions between Ag and Cu (Fig. S3).

X-ray diffraction (XRD) was conducted to confirm the crystalline structures. XRD patterns of three Ag-Cu catalysts display the same diffraction peaks at around 38.1°, 44.3°, 64.4°, and 77.5° as Ag NPs (Fig. 2a), assigned to the (111), (200), (220), and (311) planes of cubic Ag (JCPDS-04-0783). The characteristic peaks associated with copper species are hardly observed except for a tiny bump at 35.5° related to CuO (002) for Ag-Cu 5 % and Ag-Cu 10 % (Fig. 2b), due to rather weak crystallinity at low loading. Interestingly, a small downshift of Ag (111) peak position in Fig. 2b is discernible as the Cu loading increases, indicating lattice strain among the Ag-Cu catalysts, consistent with high resolution TEM results (Fig. S3).

The chemical natures of Ag and Cu were probed by using X-ray photoelectron spectroscopy (XPS). The Ag 3d spectra of three catalysts exhibit two primary doublet peaks at ~368.3 eV and ~374.3 eV, confirming the metallic state (Fig. 2c). The core-shell Ag-Cu 5 % has lower

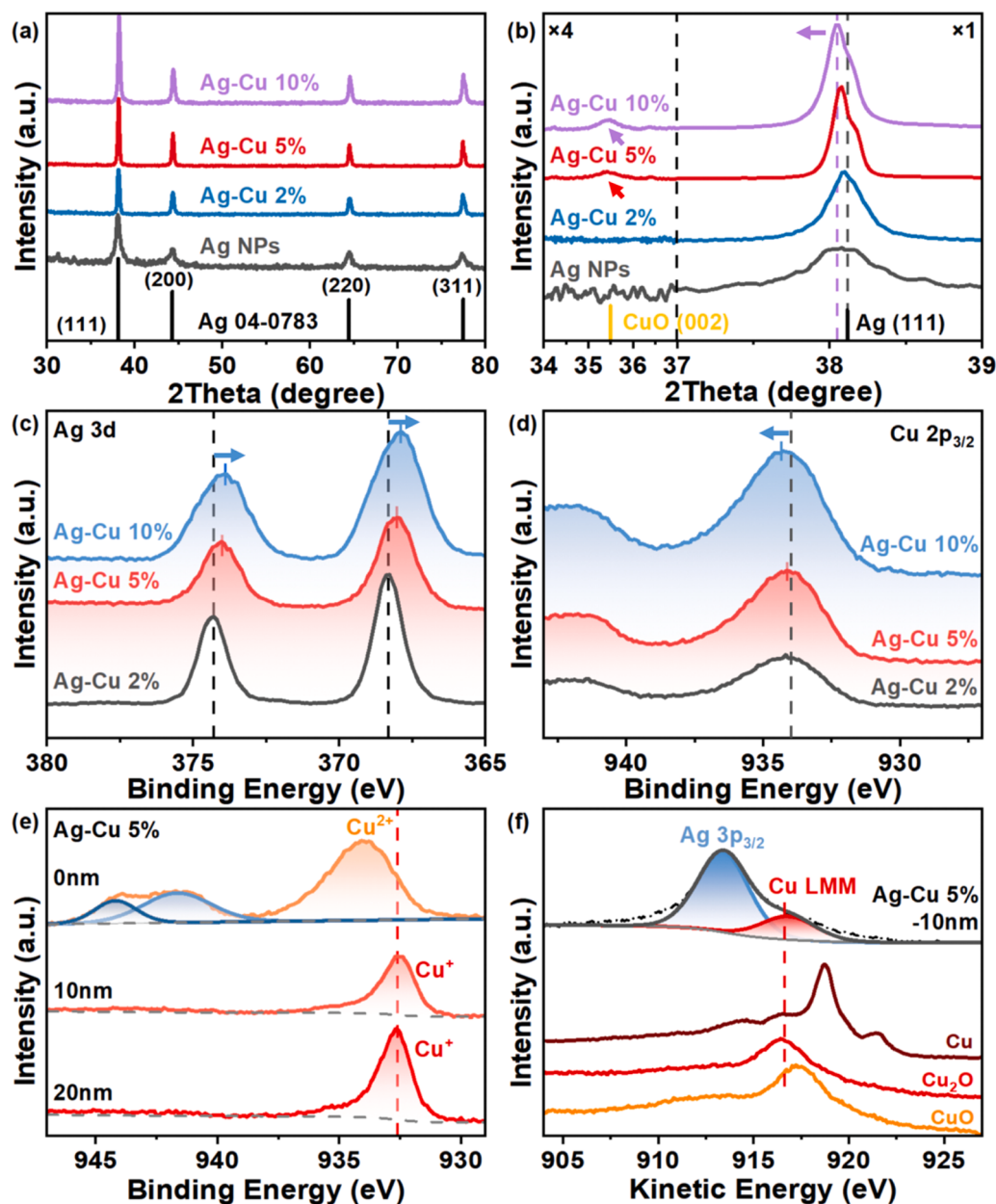


**Fig. 2.** Structure and chemical state characterizations of Ag-Cu catalysts. (a-b) XRD patterns of AgNPs, Ag-Cu 2 %, Ag-Cu 5 % and Ag-Cu 10 %. XPS spectra of (c) Ag 3d region and (d) Cu 2p<sub>3/2</sub> region for Ag-Cu 2 %, Ag-Cu 5 % and Ag-Cu 10 %. (e) XPS spectra of Cu 2p<sub>3/2</sub> region for Ag-Cu 5 % after Ar<sup>+</sup> sputter with etching depths of 0, 10 and 20 nm. (f) Cu LMM Auger spectra for Ag-Cu 5 % after Ar<sup>+</sup> sputter with etching depth of 10 nm.

peak intensities than two other catalysts due to the shield interference of Cu shell (~10 nm sampling depth estimated for the beam energy of Al K $\alpha$ ). Fig. 2d also records the Cu 2p<sub>3/2</sub> spectra having binding energies at ~933.9 eV together with the satellite features at ~942.8 eV, corresponding to the feature of Cu<sup>2+</sup>. Noticeably, with the increment of Cu loading, both Ag 3d XPS peaks have a redshift of ~0.5 eV. Meanwhile, a blue shift of Cu 2p<sub>3/2</sub> is also observed from 933.9 eV for Ag-Cu 2 % to 934.4 eV for Ag-Cu 10 %. Such phenomena consistently point to the transfer of electrons from copper to silver as the result of strong interaction between two components observed by HRTEM and XRD (Fig. 2b and S3). In order to further verify the oxidation state of Cu in the core of Ag-Cu 5 %, two sequential Ar<sup>+</sup> sputter etchings prior to XPS measurement were implemented with the removal depth of 10 nm each time. As seen in Fig. 2e, compared to CuO layer, the Cu 2p<sub>3/2</sub> peaks move to lower binding energy at ~932.6 eV together with the loss of satellite peak, suggesting the characteristic of Cu<sup>0</sup> or Cu<sup>+</sup>, which is further examined by the Auger spectra meanwhile using Cu metal, Cu<sub>2</sub>O and CuO as the references. Deconvolution of the peaks overlapped by Ag 3p<sub>3/2</sub> and Cu

LMM resolves the peak associated with copper locating at 916.5 eV, therefore corroborates the oxidation state as +1 (Fig. 2f), matching with Cu<sub>2</sub>O phase resolved by high resolution TEM images. The distinctive copper oxidation state in Ag-Cu 5 % is likely caused by the shell protecting Cu in the core being over oxidized during calcination. In addition, an apparent drop in the surface atomic Cu/Ag ratios after Ar<sup>+</sup> etching again evidences the core-shell structure of Ag-Cu 5 % while no obvious change was observed for other catalysts (Fig. S4).

From the above discussion, we can see that the rearrangement of Ag and Cu atoms during annealing as prepared Ag-Cu composite achieves the core-shell structure at Ag-Cu 5 %. Compared to the Ag-Cu 2 % (surface doping [39,40]) and Ag-Cu 10 % (disordered mixing [41,42]), the unique structure of Ag-Cu 5 % offers hierarchical interfaces, including the interactions between Ag and Cu within the core and the full-covered interactions between the core (Ag-Cu mixture) and shell (Cu layer) and gives rise to electron transferring among two segments. We expect such particular architecture and chemical potential properties would lend them exquisite catalytic performance for CO<sub>2</sub>RR.

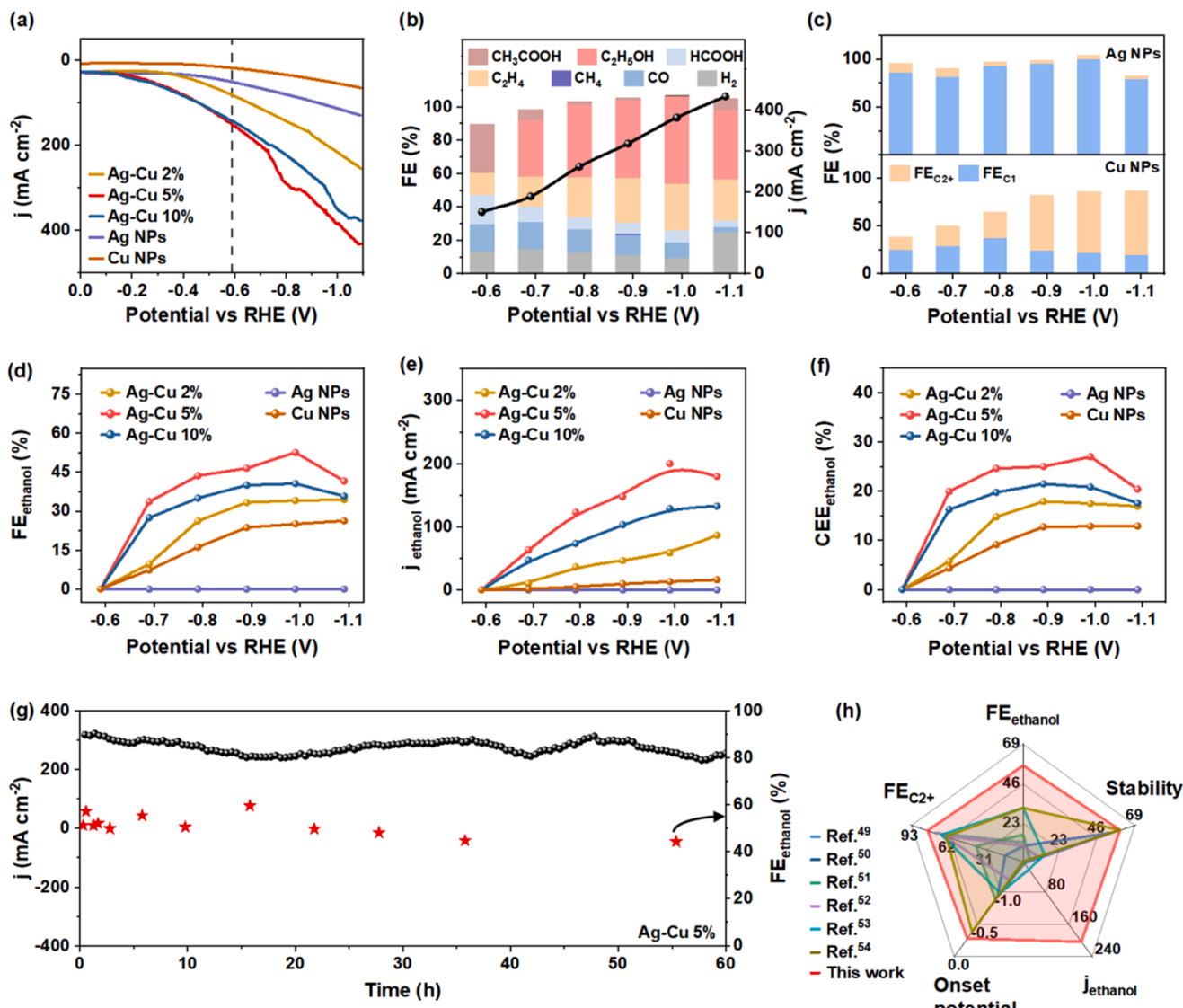


**Fig. 3.** Electrochemical CO<sub>2</sub> reduction to ethanol. (a) Linear sweep voltammetry (LSV) curves for different catalysts. (b) Faradaic efficiency (FE) values of all products and current density at various applied cathodic potentials for Ag-Cu 5 %. (c) FE values of C<sub>1</sub>, C<sub>2</sub> and current density at various applied potentials for Ag NPs and Cu NPs. (d) FEs, (e) Current density and (f) Cathodic energy efficiency (CEE) of ethanol for CO<sub>2</sub>RR over different catalysts. (g) Stability test of Ag-Cu 5 % at -0.9 V versus RHE. (h) Comparison of the onset potential, stability, FE of C<sub>2</sub> and ethanol, ethanol partial current density and half-cell CEE of the Ag-Cu 5 % catalyst with state-of-the-art results of Cu/Ag catalysts in literature.

### 3.2. Enhanced CO<sub>2</sub>RR activity toward ethanol

The Ag-Cu catalysts were immobilized on carbon paper and evaluated for the electroreduction of CO<sub>2</sub> by using a flow cell with a gas diffusion electrode (GDE) and employing 3 M aqueous KOH as the electrolyte. The bare Ag NPs, Cu NPs and Ag-CuNPs 5 % are also tested as the controls. Prior to CO<sub>2</sub>RR measurement, all the catalysts were firstly subjected to linear sweep voltammetry (LSV) in CO<sub>2</sub> or Argon atmosphere with an ohmic resistance (iR) corrections and the curves are summarized in Fig. 3a and S5. The reducing current densities ( $j$ ) show a dramatic lift compared with Ar above  $\sim -0.2$  V vs. RHE, indicating the occurrence of CO<sub>2</sub>RR. The onset potentials of Ag-Cu catalysts shift to a more positive direction than bare Ag or Cu, suggesting the reactions occur early on the Ag-Cu catalysts. A lower onset potential underlines the higher energy efficiency for core-shell Ag-Cu 5 % among the catalysts. Based on LSV results, we ran the CO<sub>2</sub>RR in the cathodic potential ranges of  $-0.6$  to  $-1.1$  V to cover the reaction zones for all samples. The gas and liquid products are identified and quantified by gas chromatography (GC) and <sup>1</sup>H nuclear magnetic resonance (<sup>1</sup>H NMR) spectroscopy. Notably, the inhabitation of hydrogen evolution reaction (HER) is evidenced by low faradaic efficiency (FE) of H<sub>2</sub> under 10 % [40, 43]. In terms of CO<sub>2</sub>RR performance, the Ag-Cu 5 % exhibits superior catalytic activity to other catalysts. Fig. 3b gives the current densities and FE of products for Ag-Cu 5 % depending on the cathodic potentials. It is intriguing that FE of total C<sub>2+</sub> products reaches 42.1 % at a rather low potential of  $-0.6$  V proving C-C coupling kinetics are enhanced. Subsequently, when the applied potentials become more negative, the FE of total C<sub>2+</sub> products gradually increase and obtain a maximum of 80.2 % at  $-1.0$  V with a high current density of  $\sim 320$  mA cm<sup>-2</sup>, in which C<sub>2</sub>H<sub>5</sub>OH accounts for 52.6 % at  $-1.0$  V (versus 27.7 % C<sub>2</sub>H<sub>4</sub>). The extraordinary FE<sub>ethanol</sub> with excellent partial current densities ( $j_{ethanol}$ ,  $\sim 173.7$  mA cm<sup>-2</sup> at  $-1.0$  V) for Ag-Cu 5 % motivates us to implement CO<sub>2</sub>RR on more control samples. The bare Ag NPs obtain dominated C<sub>1</sub> species with FE<sub>C1</sub> > 90 % throughout the applied potentials (Fig. 3c and S6). On the contrary pure Cu NPs steer the production of C<sub>2+</sub> compounds, having FE<sub>C2+</sub> > 60 % albeit with rather low  $j_{C2+}$  as 33.7 mA cm<sup>-2</sup> at  $-1.0$  V (Fig. 3c and S7), in which FE<sub>ethanol</sub> takes 25.1 %. The distinctive performance emphasizes the different electrochemical properties of Ag and Cu NPs during CO<sub>2</sub>RR. That is to say, Ag is responsible for the formation of C<sub>1</sub> intermediates, while C-C coupling is more favorable on the Cu phase, consistent with literature findings [44]. Thereby the combination of Ag and Cu could expectedly generate a synergistic approach at the interface allowing integrate of these two processes to mediate the production of C<sub>2</sub>H<sub>5</sub>OH, so-called tandem catalysis [45]. For instance, the addition of  $\sim 2$  wt. % Cu on Ag NPs (i.e., Ag-Cu 2 %) has a higher FE<sub>ethanol</sub> as 34.1 % with 58.8 mA cm<sup>-2</sup> at  $-1.0$  V (Fig. 3d, e and S8). However, the selectivity of C<sub>2</sub>H<sub>5</sub>OH and  $j_{ethanol}$  is still limited below 41 % and 128.6 mA cm<sup>-2</sup> at  $-1.0$  V for Ag-Cu 10 % with more Cu loaded (Fig. 3d, 3e and S9). Likewise, the Ag-CuNPs 5 % counterpart without core-shell structure also depicts a lower FE<sub>ethanol</sub> and  $j_{ethanol}$  of C<sub>2</sub>H<sub>5</sub>OH as 38.4 % and 83.7 mA cm<sup>-2</sup> at  $-1.0$  V (Fig. S11) than 52.6 % and 173.7 mA cm<sup>-2</sup> for Ag-Cu 5 %. Furthermore, a comprehensive literature survey found few of Ag-Cu catalysts [13, 32, 35, 42, 44, 46–54] have reported a higher FE<sub>ethanol</sub> than  $\sim 42$  % at the applied potentials from  $-0.6$  V to  $-1.0$  V in the neutral and basic circumstance (Table S2), suggesting that the synergy at the only interface between Ag and Cu is not sufficient enough to predominate C<sub>2</sub>H<sub>5</sub>OH in C<sub>2+</sub> products while one more interface constructed in Ag-Cu 5 % could provide a promotion effect [55, 56]. To prove this, we examined the electrochemical surface areas (ECSA) of Ag-Cu catalysts through the analysis of cyclic voltammograms under different scan rates (Fig. S12). An obvious higher ECSA demonstrates Ag-Cu 5 % (Double layer capacitance,  $C_{dl} = 6.27$  mF cm<sup>-1</sup>) exposes more activity due to hierarchical interfaces, which also possesses the fastest interfacial electron-transfer dynamics with the lowest interfacial charge transfer resistance ( $R_{ct}$ ) of 0.6 Ω (Fig. S13), consistent with XPS results (Fig. 2).

Moreover, the high activity and selectivity toward ethanol from CO<sub>2</sub>RR result in high energy efficiency for Ag-Cu 5 %. In Fig. 3f, a maximum half-cell cathodic energy efficiency of ethanol (see the calculation equation in Methods) is calculated as 27.0 % at  $-1.0$  V for Ag-Cu 5 %, higher than 17.5 % and 20.8 % for Ag-Cu 2 %, 10 %, respectively. The above comparisons with various controls endorse the promotion effect of hierarchical interfaces is crucial for ethanol production. Besides the activity, we also operated a long-term CO<sub>2</sub>RR on Ag-Cu 5 % at  $-0.9$  V. The duration experiment delivers a stable current of  $\sim 300$  mA cm<sup>-2</sup> and an average ethanol FE of  $\sim 50.5$  % for nearly 60 h, confirming the stability of the core-shell structure (Fig. 3g and Fig. S14). A detailed comparison to the literature under similar reaction conditions in terms of critical performance metrics, including onset potentials, FE<sub>C2+</sub>, FE<sub>ethanol</sub>,  $j_{ethanol}$  and durability further demonstrates that Ag-Cu 5 % outperforms the reported Ag-Cu catalysts for CO<sub>2</sub>RR to C<sub>2</sub>H<sub>5</sub>OH [49–54] (Fig. 3h, see more details in Table S2).

### 3.3. Understanding the enhancement of ethanol production

It is well acknowledged that the local enrichment of CO is advantageous for the multicarbon formation [44]. With this in mind, the dependence of combined C<sub>1</sub> or C<sub>2+</sub> Faradaic efficiencies on cathodic potentials is firstly elucidated in Fig. 4a for Ag-Cu 5 % catalyst. Explicitly, the population of C<sub>2+</sub> species grows when the potentials increase whereas C<sub>1</sub> species (CO dominated) follow the opposite trend. Breakdown of the C<sub>2+</sub> distribution into their main constituents reveals that the production of ethanol is favored over ethylene, as indicated by higher FE<sub>ethanol</sub> as 52.6 % than 27.7 % for FE<sub>Ethylene</sub> at  $-1.0$  V. Therefore, it is reasonable to admit that the selectivity of C<sub>2</sub>H<sub>5</sub>OH increases mainly at the expense of CO.

The analysis of active sites is crucial to investigate the enhancement of ethanol production. Fig. 4b and S15 compare selectivity and activity for CO and ethanol at  $-1.0$  V for Ag-Cu 5 % with control samples. It is observed that Ag NPs catalyzed CO<sub>2</sub>RR into 52 % CO with  $j_{CO}$  as 57.5 mA cm<sup>-2</sup> and no ethanol was detected. However, Cu NPs have  $\sim 25.1$  % ethanol with  $j_{ethanol} = 13.1$  mA cm<sup>-2</sup> albeit with much lower CO selectivity of 10.3 % (versus Ag NPs). The discerned products distribution clarifies that CO generation is more favorable on Ag than Cu while ethanol is gained only on Cu. Impregnation of Cu on Ag NPs (Ag-CuNPs 5 %) achieves more ethanol (FE<sub>ethanol</sub>,  $j_{ethanol} = 38.4$  % and 83.7 mA cm<sup>-2</sup>) than pure Cu, uncovering a promotion effect on C-C coupling, mediated by the tandem catalysis as regarded in literature [57]. That is, higher CO coverage derived on Ag could be transferred to Cu site at the interface then boost the production of multicarbon species. Interestingly, a substantially higher amount of ethanol ( $j_{ethanol} = 173.7$  mA cm<sup>-2</sup>) is obtained on core-shell Ag-Cu 5 % (Fig. 4b), confirming that multi-interfaces could provide a unique spatial (i.e., confinement) and electronical (i.e., electrons loss from Cu to Ag, Fig. 2c, d) advantages to dramatically enhance the evolution of C<sub>2</sub>H<sub>5</sub>OH.

To validate CO as intermediates during CO<sub>2</sub>RR and its improvement for ethanol evolution, we performed in-situ Raman characterization on Ag-Cu 5 %, Ag-CuNPs 5 % and Ag NPs. Fig. 4c records the spectra at the cathodic potential of  $-0.8$  V, the band emerged at 530 cm<sup>-1</sup> on Ag NPs is corresponding to the signal of Ag-CO stretching mode [45, 58], matching with high FE<sub>CO</sub> for Ag NPs (Fig. 4a, b). The intensity of this Raman peak becomes more intensive on Ag-CuNPs 5 % owing to CO<sub>2</sub> is more likely to be activated driven by coupled catalysis at the interface between Ag and Cu [59]. Ag-Cu 5 % even exhibits a maximum intensity of Ag-CO vibration, suggesting that much higher CO coverage is obtained with the benefit of core-shell structure. In addition, a relatively small peak at 375 cm<sup>-1</sup> assigned to Cu-CO stretching also appears. The distinguished intensities of CO-related peaks associated with Ag and Cu echo their different electrochemical capacity of CO<sub>2</sub>RR toward CO (Fig. 4b and S7, 8). More interesting, accompanied with the show-up of Cu-CO stretching, a weak band associated with C-H vibrational peaks on Cu is observed, which belongs to the feature of \*CHO, \*CH<sub>2</sub>CHO and

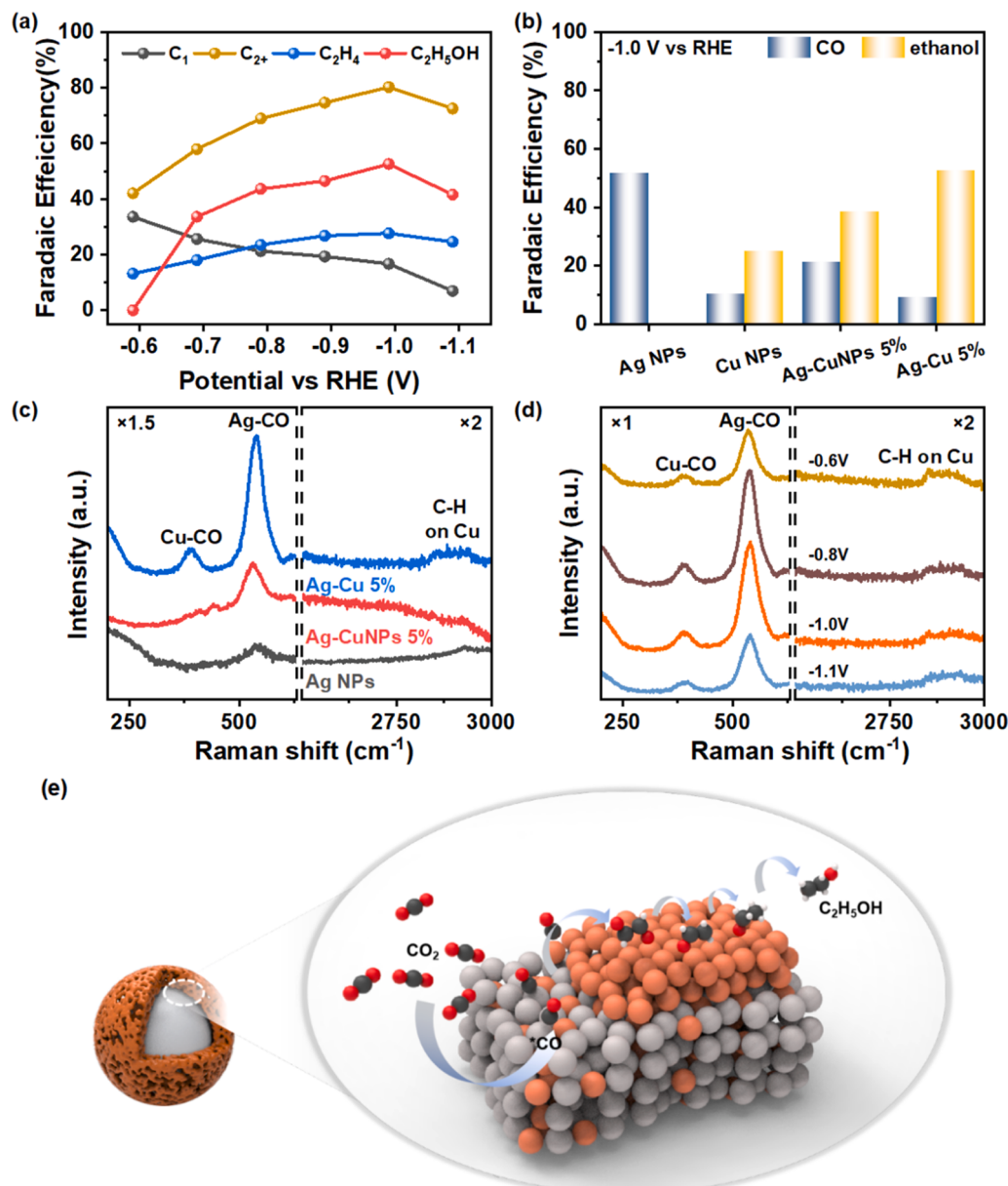


**Fig. 4.** Understanding the enhancement of ethanol production. (a) Faradaic efficiencies (FEs) of  $\text{C}_1$ ,  $\text{C}_2$ ,  $\text{C}_2\text{H}_4$  and  $\text{C}_2\text{H}_5\text{OH}$  for the Ag-Cu 5 % at various applied potentials. (b) FEs of CO and ethanol for the catalysts at -1.0 V (versus RHE). *In-situ* Raman spectra of (c) Ag-Cu 5 %, Ag-CuNPs 5 %, Ag NPs at -0.8 V (versus RHE) and (d) Ag-Cu 5 % at various applied potentials. (e) Schematic illustration of tandem catalysis for  $\text{CO}_2$ RR to  $\text{C}_2$  over core-shell Ag-Cu catalyst.

\* $\text{CH}_3\text{CHO}$  (see the transition states in the following calculation section). These species are reported as the key intermediates including in the ethanol pathway [60]. Therefore, the strong Ag-CO peak together with the obvious signals of C-H vibrations jointly point out that a higher CO amount accumulated on Ag-Cu 5 % enhances the selectivity and production rate of ethanol. It should be replenished that the absence of these peaks on Ag-CuNPs 5 % is probably low surface coverage (Fig. S10).

To probe the status of CO and other intermediates during  $\text{CO}_2$ RR for Ag-Cu 5 %, we collected the Raman spectra depending on cathodic potentials and shown in Fig. 4d. It is noted that the bands related to Ag-CO and C-H on Cu grow when the potentials become more negative and reach the topmost at -1.0 V then decrease, which is consistent with the trends of catalytic performance for  $\text{CO}_2$ RR on Ag-Cu 5 % with the superior FE<sub>ethanol</sub> and partial current density of ethanol at -1.0 V (Fig. 3b).

Based on the above results, it is reasonable to draw the scheme in Fig. 4e to illustrate the pathway that happened on core-shell Ag-Cu

ensembles, which provides the hierarchical interfaces, where  $\text{C}_1$  intermediates (e.g., CO) are enriched at the Ag dominated core, then spilled and constrained at the Cu sites at the interface of the core and Cu shell to facilitate C-C coupling preferentially to form ethanol.

### 3.4. Mechanistic investigation at atomic level

To gain more insights into the mechanism of  $\text{CO}_2$ RR on Ag-Cu 5 %, we simulated the reaction pathway by density functional theory calculations (DFT) and focused on the effect of multiple interfaces. By referring to the above characterization results and previous literature [51, 61], the structure model was reasonably simplified as Cu doped Ag(111) surface supported Cu clusters (Ag-Cu 5 %), which has appropriately contained the interface between Cu and Ag in core and another interface between Ag-Cu composite and continuous Cu surface. The similar lattice spaces of Ag surface indicated by the experimental and theoretical values (2.40 vs 2.39 Å) confirm the validity of our computational model.

The metallic state of copper in model is also verified by Auger spectra analysis of Ag-Cu 5 % post reaction (Fig. S16).

In general, the mechanism we calculated involves 12 proton-electron transfers, which including the reduction of  $\text{CO}_2$  to CO and the formation to  $\text{C}_{2+}$  products. Typically, the former phase is achieved by four proton-coupled electron transfers (PCET) for the reduction of two  $\text{CO}_2$  molecules via  $^*\text{COOH}$  ( $2^*\text{CO}_2 + 4\text{H}^+ + 4\text{e}^- \rightarrow 2^*\text{CO} + 2\text{H}_2\text{O}$ , Fig. 5a), whereas the  $\text{C}_{2+}$  production relies on the coupling and hydrogenation of two CO related intermediates [8], requiring eight proton-electron transfers, as proved by the kinetic studies and in situ Raman characterizations (Fig. 4).

For  $\text{CO}_2\text{RR}$  to CO, the lower adsorption energy of  $\text{CO}_2$  on Ag (111) surface (doped by Cu,  $-0.25$  eV) than pure Cu ( $-0.06$  eV) identifies that the electrochemical reduction is initiated on silver (Fig. S17), as higher  $\text{FE}_{\text{CO}}$  on Ag catalyst is obtained (Fig. 3c). A further comparison in terms of reaction energies ascertained for  $\text{CO}_2$  reduction to  $^*\text{CO}$  on Ag-Cu 5 % and pure Ag ( $0.58$  eV versus  $0.99$  eV, Fig. 5b) underlines that higher  $^*\text{CO}$  coverage could be expected on Ag(111) surface with Cu doped, which plays the role of the first interface in the core.

Subsequently, we investigated the reduction of  $^*\text{CO}$  to  $\text{C}_{2+}$  products (Fig. 5c). As indicated by experimental results, the tandem catalysis toward multicarbon products is implemented by migration of  $^*\text{CO}$  from Ag to Cu site, enabled by distinctive electrochemical properties of Ag and Cu during  $\text{CO}_2\text{RR}$ . Hence, we checked the  $^*\text{CO}$  adsorption on different sites and found the binding energies of  $^*\text{CO}$  on Cu are more negative ( $-0.64$  eV) than Ag ( $0.12$  eV, Fig. S18). Thus, we postulate the  $^*\text{CO}$  derived on Ag will migrate to neighboring Cu clusters and be subjected to further reduction (Fig. 5c), mimicking the process occurring at another interface between core and shell.

Given that the steric hinder causes a higher barrier ( $>1.2$  eV) [62], the conventional  $^*\text{CO}$  dimerization pathway could be excluded in our case. Instead, the formation of  $\text{C}_{2+}$  would proceed through the coupling of  $^*\text{CO}$  related hydrogenated species. Therefore, we calculated reaction energies associated with the hydrogenation of  $^*\text{CO}$  intermediates. It is found that the hydrogenation of first  $^*\text{CO}$  gives rise to  $^*\text{CHO}$  ( $0.60$  eV, Fig. 5c) rather than  $^*\text{COH}$  ( $1.39$  eV, Fig. S19). Accompanied by the

further hydrogenation, the C-C coupling occurs through a Langmuir–Hinshelwood (L-H) mechanism as  $^*\text{CHO}-\text{CHO}$  or  $^*\text{CHO}-\text{COH}$  [63], bifurcating into two possible pathways, a step found by Goddard and co-workers which is critical to control the selectivity of ethanol versus ethylene [33]. A barrier of  $0.12$  eV for C-C coupling is recognized for the ethanol pathway, much lower than that of  $0.60$  eV for ethylene, intrinsically explaining the reason for the substantially high  $\text{FE}_{\text{ethanol}}$  on Ag-Cu 5 % (Fig. 3). Besides this, we also compared the cases of two consecutive hydrogenation on same  $^*\text{CO}$  site in Fig. S20 (i.e.,  $^*\text{CO}-\text{CHOH}$ ), which also involved an elevated barrier ( $0.56$  eV). Continuously, due to a modest adsorption energy of  $^*\text{CHO}-\text{CHO}$  on Cu sites, the following hydrogenations (e.g.,  $^*\text{CHOH}-\text{CHO}$ ,  $^*\text{CH}-\text{CHO}$  etc.) proceed facilely eventually towards ethanol then closes the reaction cycle (Fig. 5c). To be different, the  $^*\text{CHO}-\text{COH}$  is susceptible to be dehydrated, producing  $^*\text{C}-\text{CHO}$ ,  $^*\text{C}-\text{CH}$  etc. until the desorption of ethylene. Moreover, the potential-determining step (PDS) in the ethanol pathway is  $^*\text{CO} + \text{H}^+ + \text{e}^- \rightarrow ^*\text{CHO}$  with a corresponding limited potential as  $0.60$  V. However, the PDS for the ethylene pathway is  $^*\text{CHO}-\text{COH} + \text{H}^+ + \text{e}^- \rightarrow ^*\text{CHO}-\text{C} + \text{H}_2\text{O}$ , requiring  $0.81$  V. The comparison of PDS again demonstrates that the Ag-Cu 5 % catalyst is more selective for  $\text{C}_2\text{H}_5\text{OH}$  formation than  $\text{C}_2\text{H}_4$ , in alignment with our experimental results. Finally, we calculated the energies associated with the C-C coupling towards ethanol based on two different models. It is noted that a lower barrier of  $0.12$  eV is found on continuous Cu surface in Ag-Cu 5 % than  $0.22$  eV on Cu doped Ag(111), which only has one type of interface between silver and copper (Fig. S21), highlighting the indispensable importance of hierarchical interface for ethanol production.

#### 4. Conclusions

We have developed a novel Ag-Cu catalyst with hierarchical interfaces for efficient  $\text{CO}_2$  electrochemical reduction to ethanol. This unique spatial structure is evolved by taking advantage of the rearrangement of metallic atoms at high temperature induced by the thermodynamic immiscibility between silver and copper. Among the

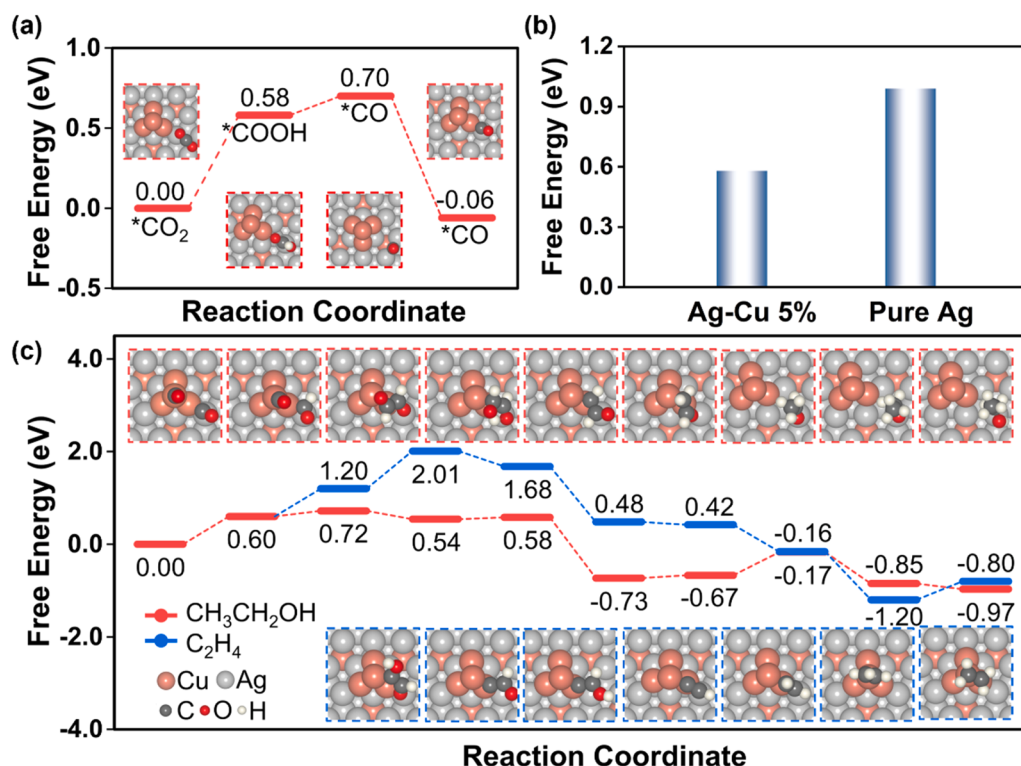


**Fig. 5.** Mechanistic investigation at atomic level. (a) The DFT calculated the free energy diagram for the reduction of  $\text{CO}_2$  to CO on Ag-Cu 5 %. The insets show the atomic structures of transition states, where the gray, orange, black, red and white represent Ag, Cu, C, O and H atoms. (b) Comparison of the free energies for the reduction of  $\text{CO}_2$  to CO on Ag-Cu 5 % and Pure Ag. (c) The DFT calculated free energy diagram for the reduction of  $^*\text{CO}$  intermediates to  $\text{C}_2$  products on Ag-Cu 5 % following  $\text{CO}_2$  reduction.

catalysts studied, the derived Ag-Cu 5 % exhibits sustainably high FE of ethanol as 52.6 % with a current density as  $\sim 320 \text{ mA cm}^{-2}$  at  $-1.0 \text{ V}$ , resulting in a cathodic energy efficiency of 27.0 % for CO<sub>2</sub>RR. The tandem catalytic process is demonstrated and ordered by local CO accumulation on Ag dominated core and subsequently energy favorable CHO-CHO occurred on continuous Cu sites towards ethanol. Our work highlights the great potential of versatile Ag-Cu interfaces in catalyzing chemical transformation and energy conversion reactions.

### CRediT authorship contribution statement

**Zhizhou Cai:** Conceptualization, Methodology, Writing - Original Draft, Visualization. **Ning Cao:** Data Curation, Writing - Original Draft. **Fanxing Zhang:** Writing - Review & Editing. **Xiangzhou Lv:** Data Curation. **Ke Wang:** Formal analysis. **Yi He:** Supervision, Project administration. **Yao Shi:** Supervision, Project administration. **Haobin Wu:** Resources. **Pengfei Xie:** Conceptualization, Writing - Review & Editing, Supervision, Funding acquisition.

### Declaration of Competing Interest

The authors declare that they have no known competing financial interests or personal relationships that could have appeared to influence the work reported in this paper.

### Data Availability

Data will be made available on request.

### Acknowledgements

This work is supported by the National Natural Science Foundation of China (22278365), Natural Science Foundation of Zhejiang Province (LR22B060002) and the grant from Shanxi-Zheda Insititue of Advanced Materials And Chemical Engineering (2021ST-AT-002). X-ray photo-electron spectroscopy (XPS) measurements was conducted by Thermo Scientific ESCALAB Xi+ at Shiyanjia lab ([www.Shiyanjia.com](http://www.Shiyanjia.com)).

### Appendix A. Supporting information

Supplementary data associated with this article can be found in the online version at [doi:10.1016/j.apcatb.2022.122310](https://doi.org/10.1016/j.apcatb.2022.122310).

### References

- [1] N.S. Spinner, J.A. Vega, W.E. Mustain, Recent progress in the electrochemical conversion and utilization of CO<sub>2</sub>, *Catal. Sci. Technol.* 2 (2012) 19–28.
- [2] J.W. Vickers, D. Alfonso, D.R. Kauffman, Electrochemical carbon dioxide reduction at nanostructured gold, copper, and alloy materials, *Energy Technol.* 5 (2017) 775–795.
- [3] Y. Zhao, Z. Pei, X.F. Lu, D. Luan, X. Wang, X.W. Lou, Rationally designed nitrogen-doped carbon macroporous fibers with loading of single cobalt sites for efficient aqueous Zn-CO<sub>2</sub> batteries, *Chem. Catal.* 2 (2022) 1480–1493.
- [4] Y. Li, S.L. Zhang, W. Cheng, Y. Chen, D. Luan, S. Gao, X.W.D. Lou, Loading single-Ni atoms on assembled hollow N-rich carbon plates for efficient CO<sub>2</sub> electroreduction, *Adv. Mater.* 34 (2022) 2105204.
- [5] D.T. Whipple, P.J.A. Kenis, Prospects of CO<sub>2</sub> utilization via direct heterogeneous electrochemical reduction, *J. Phys. Chem. Lett.* 1 (2010) 3451–3458.
- [6] Z. Yang, H. Wang, X. Fei, W. Wang, Y. Zhao, X. Wang, X. Tan, Q. Zhao, H. Wang, J. Zhu, L. Zhou, H. Ning, M. Wu, MOF derived bimetallic CuBi catalysts with ultra-wide potential window for high-efficient electrochemical reduction of CO<sub>2</sub> to formate, *Appl. Catal. B: Environ.* 298 (2021), 120571.
- [7] L. Zaza, K. Rossi, R. Buonsanti, Well-defined copper-based nanocatalysts for selective electrochemical reduction of CO<sub>2</sub> to C<sub>2</sub> products, *ACS Energy Lett.* 7 (2022) 1284–1291.
- [8] S. Nitopi, E. Bertheussen, S.B. Scott, X. Liu, A.K. Engstfeld, S. Horch, B. Seger, I.E. L. Stephens, K. Chan, C. Hahn, J.K. Nørskov, T.F. Jaramillo, I. Chorkendorff, Progress and perspectives of electrochemical CO<sub>2</sub> reduction on copper in aqueous electrolyte, *Chem. Rev.* 119 (2019) 7610–7672.
- [9] T.N. Nguyen, J. Guo, A. Sachindran, F. Li, A. Seifitokaldani, C.T. Dinh, Electrochemical CO<sub>2</sub> reduction to ethanol: from mechanistic understanding to catalyst design, *J. Mater. Chem. A* 9 (2021) 12474–12494.
- [10] Y. Hori, K. Kikuchi, S. Suzuki, Production of CO and CH<sub>4</sub> in electrochemical reduction of CO<sub>2</sub> at metal electrodes in aqueous hydrogencarbonate solution, *Chem. Lett.* 14 (1985) 1695–1698.
- [11] K.D. Yang, C.W. Lee, K. Jin, S.W. Im, K.T. Nam, Current status and bioinspired perspective of electrochemical conversion of CO<sub>2</sub> to a long-chain hydrocarbon, *J. Phys. Chem. Lett.* 8 (2017) 538–545.
- [12] H. Li, T. Liu, P. Wei, L. Lin, D. Gao, G. Wang, X. Bao, High-rate CO<sub>2</sub> electroreduction to C<sub>2+</sub> products over a copper-copper iodide catalyst, *Angew. Chem. Int. Ed.* 60 (2021) 14329–14333.
- [13] T.T.H. Hoang, S. Verma, S. Ma, T.T. Fister, J. Timoshenko, A.I. Frenkel, P.J. A. Kenis, A.A. Gewirth, Nanoporous copper-silver alloys by additive-controlled electrodeposition for the selective electroreduction of CO<sub>2</sub> to ethylene and ethanol, *J. Am. Chem. Soc.* 140 (2018) 5791–5797.
- [14] F. Hu, L. Yang, Y. Jiang, C. Duan, X. Wang, L. Zeng, X. Lv, D. Duan, Q. Liu, T. Kong, J. Jiang, R. Long, Y. Xiong, Ultrastable Cu catalyst for CO<sub>2</sub> electroreduction to multicarbon liquid fuels by tuning C-C coupling with CuTi subsurface, *Angew. Chem. Int. Ed.* 60 (2021) 26122–26127.
- [15] Q. Wan, J. Zhang, B. Zhang, D. Tan, L. Yao, L. Zheng, F. Zhang, L. Liu, X. Cheng, B. Han, Boron-doped CuO nanobundles for electroreduction of carbon dioxide to ethylene, *Green. Chem.* 22 (2020) 2750–2754.
- [16] M. Li, S. Garg, X. Chang, L. Ge, L. Li, M. Konarova, T.E. Rufford, V. Rudolph, G. Wang, Toward excellence of transition metal-based catalysts for CO<sub>2</sub> electrochemical reduction: an overview of strategies and rationales, *Small Methods* 4 (2020) 2000033.
- [17] X. Duan, J. Xu, Z. Wei, J. Ma, S. Guo, S. Wang, H. Liu, S. Dou, Metal-free carbon materials for CO<sub>2</sub> electrochemical reduction, *Adv. Mater.* 29 (2017) 1701784.
- [18] Y. Li, X.F. Lu, S. Xi, D. Luan, X. Wang, X.W.D. Lou, Synthesis of N-doped highly graphitic carbon urchin-like hollow structures loaded with single-Ni atoms towards efficient CO<sub>2</sub> electroreduction, *Angew. Chem. Int. Ed.* 61 (2022), 202201491.
- [19] Z. Li, Y. Yang, Z. Yin, X. Wei, H. Peng, K. Lyu, F. Wei, L. Xiao, G. Wang, H. D. Abruña, J. Lu, L. Zhuang, Interface-enhanced catalytic selectivity on the C<sub>2</sub> products of CO<sub>2</sub> electroreduction, *ACS Catal.* 11 (2021) 2473–2482.
- [20] Q. Shao, P. Wang, X. Huang, Opportunities and challenges of interface engineering in bimetallic nanostructure for enhanced electrocatalysis, *Adv. Funct. Mater.* 29 (2019) 1806419.
- [21] S. Zhu, E.P. Delmo, T. Li, X. Qin, J. Tian, L. Zhang, M. Shao, Recent advances in catalyst structure and composition engineering strategies for regulating CO<sub>2</sub> electrochemical reduction, *Adv. Mater.* 33 (2021) 2005484.
- [22] T. Luo, K. Liu, J. Fu, S. Chen, H. Li, J. Hu, M. Liu, Tandem catalysis on adjacent active motifs of copper grain boundary for efficient CO<sub>2</sub> electroreduction toward C<sub>2</sub> products, *J. Energy Chem.* 70 (2022) 219–223.
- [23] J.R.C. Junqueira, P.B. O'Mara, P. Wilde, S. Dieckhöfer, T.M. Benedetti, C. Andronescu, R.D. Tilley, J.J. Gooding, W. Schuhmann, Combining nanoconfinement in Ag core/porous Cu shell nanoparticles with gas diffusion electrodes for improved electrocatalytic carbon dioxide reduction, *ChemElectroChem* 8 (2021) 4848–4853.
- [24] Z.Z. Wu, X.L. Zhang, Z.Z. Niu, F.Y. Gao, P.P. Yang, L.P. Chi, L. Shi, W.S. Wei, R. Liu, Z. Chen, S. Hu, X. Zheng, M.R. Gao, Identification of Cu(100)/Cu(111) interfaces as superior active sites for CO dimerization during CO<sub>2</sub> electroreduction, *J. Am. Chem. Soc.* 144 (2022) 259–269.
- [25] Z.H. Zhao, K. Zheng, N.Y. Huang, H.L. Zhu, J.R. Huang, P.Q. Liao, X.M. Chen, A Cu (111)@metal-organic framework as a tandem catalyst for highly selective CO<sub>2</sub> electroreduction to C<sub>2</sub>H<sub>4</sub>, *Chem. Commun.* 57 (2021) 12764–12767.
- [26] C.G. Morales-Guio, E.R. Cave, S.A. Nitopi, J.T. Feaster, L. Wang, K.P. Kuhl, A. Jackson, N.C. Johnson, D.N. Abram, T. Hatsucade, C. Hahn, T.F. Jaramillo, Improved CO<sub>2</sub> reduction activity towards C<sub>2+</sub> alcohols on a tandem gold on copper electrocatalyst, *Nat. Catal.* 1 (2018) 764–771.
- [27] S.B. Varandili, D. Stoian, J. Vavra, K. Rossi, J.R. Pankhurst, Y.T. Guntern, N. Lopez, R. Buonsanti, Elucidating the structure-dependent selectivity of Cu/Zn towards methane and ethanol in CO<sub>2</sub> electroreduction using tailored Cu/ZnO precatalysts, *Chem. Sci.* 12 (2021) 14484–14493.
- [28] L. Wan, X. Zhang, J. Cheng, R. Chen, L. Wu, J. Shi, J. Luo, Bimetallic Cu-Zn catalysts for electrochemical CO<sub>2</sub> reduction: phase-separated versus core-shell distribution, *ACS Catal.* 12 (2022) 2741–2748.
- [29] H. Xie, F. Wang, T. Liu, Y. Wu, C. Lan, B. Chen, J. Zhou, B. Chen, Copper-iron dimer for selective C-C coupling in electrochemical CO<sub>2</sub> reduction, *Electrochim. Acta* 380 (2021), 138188.
- [30] S. Verma, B. Kim, H.R. Jhong, S. Ma, P.J. Kenis, A gross-margin model for defining technoeconomic benchmarks in the electroreduction of CO<sub>2</sub>, *ChemSusChem* 9 (2016) 1972–1979.
- [31] Y.C. Li, Z. Wang, T. Yuan, D.H. Nam, M. Luo, J. Wicks, B. Chen, J. Li, F. Li, F.P. G. de Arquer, Y. Wang, C.T. Dinh, O. Voznyy, D. Sinton, E.H. Sargent, Binding site diversity promotes CO<sub>2</sub> electroreduction to ethanol, *J. Am. Chem. Soc.* 141 (2019) 8584–8591.
- [32] F. Li, Y.C. Li, Z. Wang, J. Li, D.H. Nam, Y. Lum, M. Luo, X. Wang, A. Ozden, S. Hwang, B. Chen, Y. Wang, J. Wicks, Y. Xu, Y. Li, C.M. Gabardo, C.T. Dinh, Y. Wang, T.T. Zhuang, D. Sinton, E.H. Sargent, Cooperative CO<sub>2</sub>-to-ethanol conversion via enriched intermediates at molecule-metal catalyst interfaces, *Nat. Catal.* 3 (2019) 75–82.
- [33] H. Xiao, T. Cheng, W.A. Goddard 3rd, Atomistic mechanisms underlying selectivities in C(1) and C(2) products from electrochemical reduction of CO on Cu (111), *J. Am. Chem. Soc.* 139 (2017) 130–136.
- [34] E.L. Clark, C. Hahn, T.F. Jaramillo, A.T. Bell, Electrochemical CO<sub>2</sub> reduction over compressively strained CuAg surface alloys with enhanced multi-carbon oxygenate selectivity, *J. Am. Chem. Soc.* 139 (2017) 15848–15857.

[35] C.P. Yang, B.H. Ko, S. Hwang, Z.Y. Liu, Y.G. Yao, W. Luc, M.J. Cui, A.S. Malkani, T. Y. Li, X.Z. Wang, J.Q. Dai, B.J. Xu, G.F. Wang, D. Su, F. Jiao, L.B. Hu, Overcoming immiscibility toward bimetallic catalyst library, *Sci. Adv.* 6 (2020) eaaz6844.

[36] Y. Qin, Y.T. Wang, H.B. Yang, W. Zhu, Recent advances on the construction of diarylethene-based supramolecular metallacycles and metallacages via coordination-driven self-assembly, *Chem. Synth.* 1 (2021) 2.

[37] P. Xie, J. Ding, Z. Yao, T. Pu, P. Zhang, Z. Huang, C. Wang, J. Zhang, N. Zecher-Freeman, H. Zong, D. Yuan, S. Deng, R. Shahbazian-Yassar, C. Wang, Oxo dicopper anchored on carbon nitride for selective oxidation of methane, *Nat. Commun.* 13 (2022) 1375.

[38] J.M. Zhang, G.X. Chen, K.W. Xu, Atomistic study of self-diffusion in Cu-Ag immiscible alloy system, *J. Alloy. Compd.* 425 (2006) 169–175.

[39] C.W. Hung, C.C. Wang, W.J. Li, I.C. Cheng, Synthesis of bimetallic catalysts using Ag extracted from end-of-life solar modules supported on nanoporous Cu for electrochemical CO<sub>2</sub> reduction, *J. Phys. Chem. Solids* 166 (2022), 110707.

[40] X. Lv, L. Shang, S. Zhou, S. Li, Y. Wang, Z. Wang, T.K. Sham, C. Peng, G. Zheng, Electron-deficient Cu sites on Cu<sub>3</sub>Ag<sub>1</sub> catalyst promoting CO<sub>2</sub> electroreduction to alcohols, *Adv. Energy Mater.* 10 (2020) 2001987.

[41] S. Lee, G. Park, J. Lee, Importance of Ag-Cu biphasic boundaries for selective electrochemical reduction of CO<sub>2</sub> to ethanol, *ACS Catal.* 7 (2017) 8594–8604.

[42] A. Vasiljeff, C. Xu, Y. Jiao, Y. Zheng, S.-Z. Qiao, Surface and interface engineering in copper-based bimetallic materials for selective CO<sub>2</sub> electroreduction, *Chem* 4 (2018) 1809–1831.

[43] J.A. Gauthier, Z. Lin, M. Head-Gordon, A.T. Bell, Pathways for the formation of C<sub>2+</sub> products under alkaline conditions during the electrochemical reduction of CO<sub>2</sub>, *ACS Energy Lett.* 7 (2022) 1679–1686.

[44] C.B. Chen, Y.F. Li, S. Yu, S. Louisiana, J.B. Jin, M.F. Li, M.B. Ross, P.D. Yang, Cu-Ag tandem catalysts for high-rate CO<sub>2</sub> electrolysis toward multicarbons, *Joule* 4 (2020) 1688–1699.

[45] J. Gao, H. Zhang, X. Guo, J. Luo, S.M. Zakeeruddin, D. Ren, M. Gratzel, Selective C-C coupling in carbon dioxide electroreduction via efficient spillover of intermediates as supported by operando Raman spectroscopy, *J. Am. Chem. Soc.* 141 (2019) 18704–18714.

[46] Y. Xu, C. Li, Y. Xiao, C. Wu, Y. Li, Y. Li, J. Han, Q. Liu, J. He, Tuning the selectivity of liquid products of CO<sub>2</sub>RR by Cu-Ag alloying, *Acs. Appl. Mater. Interfaces* 14 (2022) 11567–11574.

[47] Z. Chang, S. Huo, W. Zhang, J. Fang, H. Wang, The tunable and highly selective reduction products on Ag@Cu bimetallic catalysts toward CO<sub>2</sub> electrochemical reduction reaction, *J. Phys. Chem. C* 121 (2017) 11368–11379.

[48] J. Huang, M. Mensi, E. Oveisi, V. Mantella, R. Buonsanti, Structural sensitivities in bimetallic catalysts for electrochemical CO<sub>2</sub> reduction revealed by Ag-Cu nanodimers, *J. Am. Chem. Soc.* 141 (2019) 2490–2499.

[49] Y. Zhong, X. Kong, Z. Song, Y. Liu, L. Peng, L. Zhang, X. Luo, J. Zeng, Z. Geng, Adjusting local CO confinement in porous-shell Ag@Cu catalysts for enhancing C-C coupling toward CO<sub>2</sub> eletroreduction, *Nano Lett.* 22 (2022) 2554–2560.

[50] C.J. Chang, S.C. Lin, H.C. Chen, J. Wang, K.J. Zheng, Y. Zhu, H.M. Chen, Dynamic reoxidation/reduction-driven atomic interdiffusion for highly selective CO<sub>2</sub> reduction toward methane, *J. Am. Chem. Soc.* 142 (2020) 12119–12132.

[51] L.R.L. Ting, O. Piqué, S.Y. Lim, M. Tanhaei, F. Calle-Vallejo, B.S. Yeo, Enhancing CO<sub>2</sub> electroreduction to ethanol on copper-silver composites by opening an alternative catalytic pathway, *ACS Catal.* 10 (2020) 4059–4069.

[52] Y. Ma, J. Yu, M. Sun, B. Chen, X. Zhou, C. Ye, Z. Guan, W. Guo, G. Wang, S. Lu, D. Xia, Y. Wang, Z. He, L. Zheng, Q. Yun, L. Wang, J. Zhou, P. Lu, J. Yin, Y. Zhao, Z. Luo, L. Zhai, L. Liao, Z. Zhu, R. Ye, Y. Chen, Y. Lu, S. Xi, B. Huang, C.S. Lee, Z. Fan, Confined growth of silver-copper Janus nanostructures with {100} facets for highly selective tandem electrocatalytic carbon dioxide reduction, *Adv. Mater.* 34 (2022) 2110607.

[53] S. Zhang, S. Zhao, D. Qu, X. Liu, Y. Wu, Y. Chen, W. Huang, Electrochemical reduction of CO<sub>2</sub> toward C<sub>2</sub> valuables on Cu@Ag core-shell tandem catalyst with tunable shell thickness, *Small* 17 (2021) 2102293.

[54] Y. Xia, Q. Zhang, F. Guo, J. Wang, W. Li, J. Xu, Ag@Cu with Cu-CuO interface prepared by air cold-plasma promoting the electrocatalytic reduction of CO<sub>2</sub> to low-carbon alcohols, *Vacuum* 196 (2022), 110767.

[55] S. Nag, K.C. Mahdak, A. Devaraj, S. Gohil, P. Ayub, R. Banerjee, Phase separation in immiscible silver-copper alloy thin films, *J. Mater. Sci.* 44 (2009) 3393–3401.

[56] J. Wang, Z. Li, C. Dong, Y. Feng, J. Yang, H. Liu, X. Du, Silver/copper interface for relay electroreduction of carbon dioxide to ethylene, *ACS Appl. Mater. Interfaces* 11 (2019) 2763–2767.

[57] P. Iyengar, M.J. Kolb, J.R. Pankhurst, F. Calle-Vallejo, R. Buonsanti, Elucidating the facet-dependent selectivity for CO<sub>2</sub> electroreduction to ethanol of Cu-Ag tandem catalysts, *ACS Catal.* 11 (2021) 4456–4463.

[58] A. Herzog, A. Bergmann, H.S. Jeon, J. Timoshenko, S. Kuhl, C. Rettenmaier, M. Lopez Luna, F.T. Haase, B. Roldan Cuenya, Operando investigation of Ag-decorated Cu<sub>2</sub>O nanocube catalysts with enhanced CO<sub>2</sub> electroreduction toward liquid products, *Angew. Chem. Int. Ed.* 60 (2021) 7426–7435.

[59] H. Huang, H. Song, J. Kou, C. Lu, J. Ye, Atomic-level insights into surface engineering of semiconductors for photocatalytic CO<sub>2</sub> reduction, *J. Energy Chem.* 67 (2022) 309–341.

[60] G.M. Tomboe, S. Choi, T. Kwon, Y.J. Hwang, K. Lee, Potential link between Cu surface and selective CO<sub>2</sub> electroreduction: perspective on future electrocatalyst designs, *Adv. Mater.* 32 (2020) 1908398.

[61] Z. Zhang, G. Wen, D. Luo, B. Ren, Y. Zhu, R. Gao, H. Dou, G. Sun, M. Feng, Z. Bai, A. Yu, Z. Chen, Two ships in a bottle" design for Zn-Ag-O catalyst enabling selective and long-lasting CO<sub>2</sub> electroreduction, *J. Am. Chem. Soc.* 143 (2021) 6855–6864.

[62] T.K. Todorova, M.W. Schreiber, M. Fontecave, Mechanistic understanding of CO<sub>2</sub> reduction reaction (CO<sub>2</sub>RR) toward multicarbon products by heterogeneous copper-based catalysts, *ACS Catal.* 10 (2019) 1754–1768.

[63] A.J. Garza, A.T. Bell, M. Head-Gordon, Mechanism of CO<sub>2</sub> reduction at copper surfaces: pathways to C<sub>2</sub> products, *ACS Catal.* 8 (2018) 1490–1499.